MSW MANAGEMENT -Multidisciplinary, Scientific Work and Management Journal
ISSN: 1053-7899
Vol. 36 Issue 1, Jan-June 2026, Pages: 1117-1129

Structural and electrical properties of sol–gel grown $Zn_{0.95}Mn_{0.05}O$ nanoparticles

Mukesh Tiwari [a], M.J. Keshvani [b], P.V. Kanjariya [a]

[a] Department of Physics, Marwadi University, 360003, India
[b] The Patidar Gin Science College, Bardoli, 394601, India
Email: prakash.kanjariya@marwadieducation.edu.in

Abstract

The structural and electrical properties of the synthesized Mn–doped ZnO–based sample were systematically investigated. X–ray diffraction (XRD) analysis confirmed the formation of a single–phase polycrystalline wurtzite structure, indicating high crystallinity and phase purity. Temperature–dependent measurements revealed that the refractive index and maximum barrier height decrease with increasing temperature, suggesting enhanced carrier mobility at elevated temperatures. DC resistivity was measured under varying applied currents (0.2 mA, 1 mA, and 5 mA), showing a strong dependence on both temperature and current. To analyze the conduction mechanism, the resistivity data were fitted using a combined Variable Range Hopping (VRH) and Small Polaron Conduction (SPC) model. Activation energies extracted from the fitting indicate that VRH governs long–range hopping between localized states, whereas SPC represents nearest–neighbor polaron hopping. Both activation energies decrease with increasing current, reflecting facilitated carrier transport under higher applied fields. The combined VRH + SPC model accurately describes the DC resistivity behavior of the samples, confirming thermally activated current–dependent conduction.

Keywords
Mn–doped ZnO; X–ray diffraction; dielectric; ac conductivity; dc resistivity.

Introduction

In recent decades, functional metal oxide nanomaterials have attracted immense scientific and technological interest due to their size–dependent physical, chemical, and electronic properties, which differ significantly from their bulk counterparts. The reduction of material dimensions to the nanoscale introduces quantum confinement effects, enhanced surface–to–volume ratios, and modified defect structures, enabling tunable optical, electrical, magnetic, and catalytic characteristics. These features make metal oxide nanoparticles promising candidates for a wide range of applications including optoelectronic devices, transparent conducting electrodes, sensors, photocatalysts, spintronic components, and energy harvesting systems. Among various metal oxides, zinc oxide (ZnO) has emerged as one of the most extensively studied semiconductor materials owing to its unique combination of wide band gap, high exciton binding energy, excellent chemical stability, and environmental friendliness [1–3].

ZnO is a II–VI compound semiconductor crystallizing predominantly in the hexagonal wurtzite structure under ambient conditions. It possesses a wide direct band gap of approximately 3.37 eV at room temperature and a large exciton binding energy of about 60 meV, which ensures efficient excitonic emission even at elevated temperatures. These intrinsic properties make ZnO a promising material for ultraviolet light emitters, photodetectors, laser diodes, and transparent electronics. In addition, ZnO exhibits high optical transparency in the visible region, good piezoelectric characteristics, and remarkable thermal and chemical stability. The abundance, low cost, and non–toxicity of zinc further enhance the attractiveness of ZnO for large–scale device fabrication [4–6].

Despite its favorable intrinsic properties, the electrical behavior of ZnO is strongly influenced by native point defects such as oxygen vacancies (V_O), zinc interstitials (Zn_i), and zinc vacancies (V_{Zn}). These defects often lead to unintentional n–type conductivity in ZnO, which poses challenges for achieving stable and reproducible p–type doping. The electrical conductivity, carrier concentration, and mobility of ZnO can be tailored by controlling synthesis conditions, particle size, defect density, and dopant incorporation. Understanding and engineering these parameters are crucial for optimizing ZnO–based devices, particularly in applications where controlled electrical transport and charge carrier dynamics are required [7–9].

One of the most effective approaches to modify the structural, optical, electrical, and magnetic properties of ZnO is substitutional doping with suitable foreign ions. Both non–metal and metal dopants have been extensively investigated to tailor the band structure, defect chemistry, and charge transport behavior of ZnO. Transition metal (TM) dopants such as Mn, Co, Fe, Ni, and Cr are of particular interest due to their ability to introduce localized magnetic moments and alter the electronic structure of ZnO. Doping with TM ions can lead to enhanced electrical conductivity, modified band gap energy, and the emergence of dilute magnetic semiconductor (DMS) behavior, which is highly desirable for spintronics and multifunctional device applications [10–12].

Among various transition metal dopants, manganese (Mn) has received significant attention due to its multiple valence states (Mn^{2+}, Mn^{3+}, Mn^{4+}), high magnetic moment, and ionic radius comparable to that of Zn^{2+}. The ionic radius of Mn^{2+} (0.80 Å) is close to that of Zn^{2+} (0.74 Å), which facilitates substitutional incorporation of Mn ions at Zn lattice sites without causing severe lattice distortion at low doping concentrations. Mn doping has been reported to influence the crystal structure, grain size, defect concentration, electrical conductivity, and magnetic ordering of ZnO. Consequently, Mn–doped ZnO has emerged as a promising material system for magneto–optoelectronic and spintronic applications [13–15].

MSW MANAGEMENT -Multidisciplinary, Scientific Work and Management Journal
ISSN: 1053-7899
Vol. 36 Issue 1, Jan-June 2026, Pages: 1117-1129

The incorporation of Mn ions into the ZnO lattice can significantly affect the structural characteristics of the host material. Substitutional Mn doping may induce lattice strain, modify lattice parameters, and influence crystallite growth kinetics. Several studies have reported that low–level Mn doping preserves the wurtzite structure of ZnO while causing slight shifts in X–ray diffraction peak positions due to lattice expansion or contraction. At higher doping concentrations, secondary phases such as MnO, Mn_3O_4, or $ZnMn_2O_4$ may appear, which can deteriorate the desired physical properties. Therefore, controlling the dopant concentration and synthesis method is essential to achieve single–phase Mn–doped ZnO nanoparticles with improved functional performance [16–18].

The electrical properties of Mn–doped ZnO are governed by a complex interplay between dopant–induced states, native defects, and microstructural features. Mn incorporation can modify the carrier concentration by altering defect equilibria, particularly oxygen vacancies and zinc interstitials. Depending on the synthesis conditions and Mn concentration, Mn doping may either enhance or suppress electrical conductivity. Studies have shown that Mn–doped ZnO often exhibits semiconducting behavior with temperature–dependent conductivity following Arrhenius or variable–range hopping mechanisms. A detailed understanding of charge transport processes in Mn–doped ZnO nanoparticles is critical for their application in sensors, transparent electronics, and multifunctional devices [19–21].

At the nanoscale, the structural and electrical properties of ZnO–based materials are further influenced by particle size, surface states, and grain boundary effects. Nanoparticles possess a large density of surface defects and grain boundaries, which can act as trapping centers for charge carriers and significantly affect electrical transport. The interaction between Mn dopants and surface–related defects becomes increasingly important in nanostructured systems. As a result, Mn–doped ZnO nanoparticles often exhibit properties distinct from those of bulk or thin–film counterparts, underscoring the need for systematic experimental investigations focusing specifically on nanoparticle systems [22–24].

Among various synthesis techniques such as hydrothermal, co–precipitation, chemical vapor deposition, and pulsed laser deposition, the sol–gel method has emerged as a versatile and cost–effective route for the preparation of doped ZnO nanoparticles. The sol–gel technique offers several advantages including low processing temperature, precise control over stoichiometry, uniform dopant distribution, high chemical homogeneity, and scalability. Moreover, sol–gel synthesis allows fine tuning of particle size and morphology through careful control of precursor concentration, pH, aging time, and calcination conditions. These features make the sol–gel method particularly suitable for preparing Mn–doped ZnO nanoparticles for systematic structure–property correlation studies [25–27].

Although numerous studies have investigated Mn–doped ZnO systems, discrepancies remain regarding the influence of Mn concentration on structural integrity and electrical behavior. Some reports suggest enhanced conductivity due to increased oxygen vacancy concentration, while others indicate carrier localization and reduced conductivity due to defect clustering or grain boundary effects. Furthermore, many studies focus primarily on optical or magnetic properties, with comparatively fewer reports providing detailed analysis of electrical transport mechanisms in sol–gel synthesized Mn–doped ZnO nanoparticles. In particular, systematic studies correlating low–level Mn substitution (≈5 at.%) with crystallographic parameters, microstructural evolution, and temperature–dependent electrical behavior are still limited [28–30].

The choice of $Zn_{0.95}Mn_{0.05}O$ composition is motivated by the need to introduce sufficient Mn ions to modify the electrical and structural properties while avoiding the formation of secondary impurity phases. A doping concentration of 5 mol% is often considered optimal for achieving substitutional incorporation of Mn^{2+} ions into the ZnO lattice without significantly disrupting the wurtzite structure. At this concentration, meaningful changes in lattice parameters, crystallite size, defect density, and charge transport behavior can be observed, making it an ideal composition for fundamental and applied investigations [31–33].

In addition to temperature–dependent electrical transport, the influence of applied current on resistivity provides important insight into charge carrier dynamics and conduction mechanisms in nanostructured semiconductors. At the nanoscale, electrical transport may deviate from ideal ohmic behavior due to grain boundary barriers, defect states, Joule heating, and field–assisted carrier hopping. Current–dependent resistivity measurements are therefore valuable for distinguishing between thermally activated conduction, space–charge–limited conduction, and hopping–based transport mechanisms. Despite their significance, systematic investigations combining temperature– and current–dependent resistivity in Mn–doped ZnO nanoparticles remain relatively limited, particularly for sol–gel synthesized systems. Incorporating such measurements enables a more comprehensive understanding of dopant–defect interactions and charge transport behavior in ZnO–based nanomaterials.

In this context, a comprehensive experimental investigation of the structural and electrical properties of sol–gel grown $Zn_{0.95}Mn_{0.05}O$ nanoparticles is both scientifically relevant and technologically important. Detailed structural analysis using X–ray diffraction can provide insights into phase purity, crystallite size, lattice strain, and dopant incorporation. Electrical characterization over a wide temperature range can reveal the dominant charge transport mechanisms and the role of Mn–induced defects. Such studies contribute to a deeper understanding of dopant–defect interactions in ZnO–based nanomaterials and support the rational design of materials for electronic and spintronic applications.

The primary objective of the present work is to synthesize high–quality $Zn_{0.95}Mn_{0.05}O$ nanoparticles using the sol–gel method and to systematically investigate their structural and electrical properties. The study aims to (i) confirm the successful incorporation of Mn into the ZnO lattice without secondary phase formation, (ii) analyze the effect of Mn doping on crystallite size and lattice parameters, and (iii) examine the temperature–dependent electrical behavior to elucidate the underlying

MSW MANAGEMENT -Multidisciplinary, Scientific Work and Management Journal
ISSN: 1053-7899
Vol. 36 Issue 1, Jan-June 2026, Pages: 1117-1129

conduction mechanisms. The results of this study are expected to provide valuable insights into the structure–property relationships of Mn–doped ZnO nanoparticles and to highlight their potential for advanced functional device applications.

Experimental details

Materials and chemicals

All chemicals used in the present investigation were of analytical reagent (AR) grade and were used without further purification. Zinc acetate dihydrate ($Zn(CH_3COO)_2 \cdot 2H_2O$) was employed as the zinc precursor, while manganese acetate tetrahydrate ($Mn(CH_3COO)_2 \cdot 4H_2O$) was used as the manganese dopant source. Absolute ethanol was used as the solvent, and monoethanolamine (MEA) served as a stabilizing and complexing agent. Deionized water was used wherever required during the synthesis process.

Synthesis of $Zn_{0.95}Mn_{0.05}O$ nanoparticles

$Zn_{0.95}Mn_{0.05}O$ nanoparticles were synthesized using a conventional sol–gel route due to its simplicity, low processing temperature, and ability to provide homogeneous dopant distribution. Initially, a stoichiometric amount of zinc acetate dihydrate was dissolved in absolute ethanol under constant magnetic stirring at room temperature to form a clear solution. Separately, manganese acetate tetrahydrate corresponding to 5 mol% Mn concentration was dissolved in ethanol and added slowly to the zinc precursor solution.

Monoethanolamine was then added dropwise to the mixed solution as a stabilizer, maintaining a molar ratio of MEA to total metal ions of 1:1. The resulting solution was stirred continuously for several hours until a transparent and homogeneous sol was obtained. The sol was then aged at room temperature for 24 h to promote hydrolysis and polycondensation reactions.

After aging, the sol was heated at moderate temperature to remove the solvent and initiate gel formation. The obtained gel was dried in an oven at approximately 100–120 °C to eliminate residual organic components and moisture. The dried precursor was then finely ground and calcined in air at an optimized temperature (typically 400–500 °C) for several hours to achieve crystallization of $Zn_{0.95}Mn_{0.05}O$ nanoparticles. The calcination temperature and duration were carefully selected to ensure phase purity and to avoid the formation of secondary manganese oxide phases.

Structural characterization

The crystal structure, phase purity, and crystallographic parameters of the synthesized $Zn_{0.95}Mn_{0.05}O$ nanoparticles were investigated using X–ray diffraction (XRD). XRD patterns were recorded using a powder X–ray diffractometer equipped with Cu Kα radiation (λ = 1.5406 Å), operated at appropriate accelerating voltage and current. The diffraction data were collected over a wide 2θ range, typically from 20° to 70°, with a suitable step size and scanning rate.

The average crystallite size of the nanoparticles was estimated from the most intense diffraction peaks using the Scherrer formula. Lattice parameters were calculated using standard indexing methods, and peak position shifts were analyzed to assess the incorporation of Mn ions into the ZnO lattice. The absence of additional diffraction peaks corresponding to secondary phases was used to confirm the formation of single–phase Mn–doped ZnO with wurtzite structure.

Electrical measurements

The electrical properties of $Zn_{0.95}Mn_{0.05}O$ nanoparticles were studied using temperature–dependent dc electrical conductivity measurements. For this purpose, the synthesized nanopowder was pressed into circular pellets of uniform thickness using a hydraulic press under high pressure. The pellets were subsequently sintered at an optimized temperature to improve mechanical strength and electrical contact between grains.

Ohmic contacts were formed on both flat surfaces of the pellets using conductive silver paste. The dc electrical conductivity measurements were carried out using a two–probe method over a wide temperature range. The samples were mounted in a temperature–controlled chamber, and the temperature was varied gradually to ensure thermal equilibrium at each measurement point.

The electrical conductivity (σ) was calculated using the relation $\sigma = L / (RA)$, where L is the thickness of the pellet, A is the cross–sectional area, and R is the measured electrical resistance. The temperature dependence of conductivity was analyzed to understand the charge transport mechanism and the influence of Mn doping on the electrical behavior of ZnO nanoparticles.

Temperature– and current–dependent resistivity measurements

Temperature–dependent resistivity measurements were carried out under different applied current values to investigate the influence of electric field and current density on charge transport behavior. Pelletized $Zn_{0.95}Mn_{0.05}O$ samples with silver–coated electrodes were used for these measurements. dc resistivity was measured using a two–probe configuration while applying constant current values in a controlled manner.

The resistivity measurements were performed over a wide temperature range at several fixed current levels to ensure stable and reproducible data. At each temperature, sufficient time was allowed for thermal equilibrium before recording the voltage drop across the sample. Care was taken to minimize contact resistance and Joule heating effects by selecting appropriate current values and ensuring linear current–voltage characteristics within the measurement range.

The electrical resistivity (ρ) was calculated using the relation $\rho = RA / L$, where R is the measured resistance, A is the cross–sectional area of the pellet, and L is its thickness. The variation of resistivity with temperature under different applied currents was analyzed to identify possible deviations from ohmic behavior and to understand the role of grain boundaries, defect states, and Mn–induced localized levels in the conduction process.

MSW MANAGEMENT -Multidisciplinary, Scientific Work and Management Journal
ISSN: 1053-7899
Vol. 36 Issue 1, Jan-June 2026, Pages: 1117-1129

The combined analysis of temperature– and current–dependent resistivity data provides deeper insight into the dominant charge transport mechanisms and helps distinguish between thermally activated conduction and field–assisted hopping processes in Mn–doped ZnO nanoparticles.

Analysis of conduction mechanism

To elucidate the dominant electrical conduction mechanism, the temperature–dependent conductivity data were analyzed using appropriate theoretical models such as Arrhenius–type thermally activated conduction and hopping conduction models. Activation energy values were extracted from the slope of ln(σ) versus inverse temperature plots in different temperature regions. The obtained results were correlated with structural parameters, defect states, and dopant incorporation to understand the role of Mn ions and grain boundaries in charge transport.

Experimental reproducibility

All synthesis and characterization experiments were repeated to ensure reproducibility of the results. Consistent structural and electrical behavior observed across multiple samples confirmed the reliability of the sol–gel synthesis process and the stability of the $Zn_{0.95}Mn_{0.05}O$ nanoparticle system.

Results and discussion

Structural properties

The X–ray diffraction (XRD) pattern of the synthesized $Zn_{0.95}Mn_{0.05}O$ nanoparticles is shown in Fig. 1. The diffraction peaks observed at 2θ values corresponding to the (100), (002), (101), (102), (110), (103), and (112) planes confirm that the sample crystallizes in the hexagonal wurtzite structure of ZnO, in good agreement with the standard JCPDS card no. 36–1451 [34]. No additional peaks related to secondary phases such as MnO, Mn_2O_3, Mn_3O_4, or $ZnMn_2O_4$ are detected, indicating the formation of a single–phase Mn–doped ZnO material.

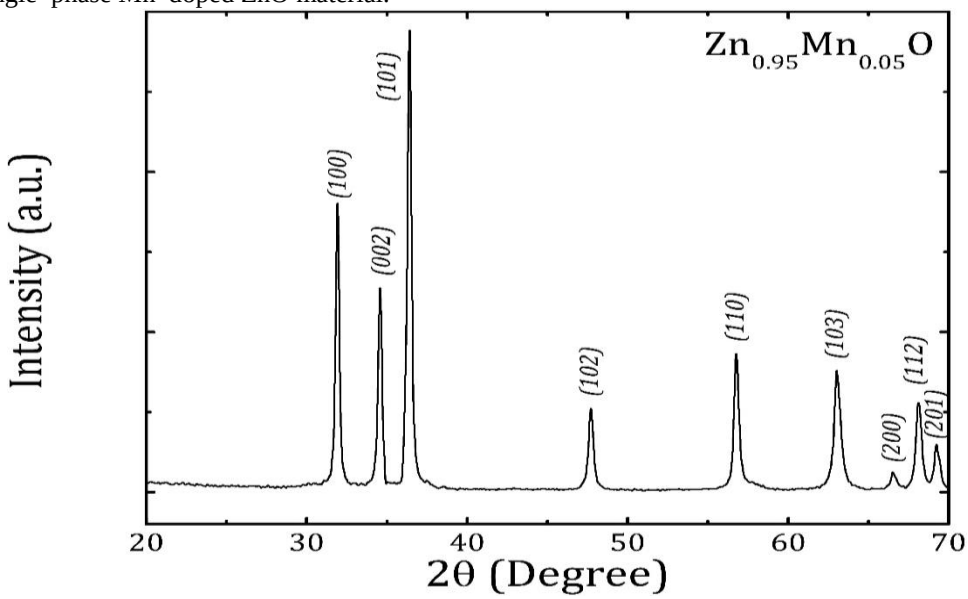

Figure 1: XRD Pattern with (hkl) crystallographic directions for $Zn_{0.95}Mn_{0.05}O$ nanoparticles

The absence of impurity peaks demonstrates that Mn ions are successfully incorporated into the ZnO lattice rather than forming segregated manganese oxide phases. Similar phase–pure wurtzite structures have been reported for Mn–doped ZnO synthesized by sol–gel and other chemical routes at comparable dopant concentrations [35–37]. Compared to pristine ZnO reported in the literature [34,38], a slight shift in diffraction peak positions is observed in the Mn–doped sample. In particular, the major diffraction peaks exhibit a marginal shift toward lower 2θ angles, which suggests an expansion of the ZnO lattice due to Mn incorporation. This behavior is attributed to the substitution of Zn^{2+} ions (ionic radius ≈ 0.74 Å) by slightly larger Mn^{2+} ions (ionic radius ≈ 0.80 Å) at tetrahedral lattice sites [39]. Such peak shifts upon Mn doping have been consistently observed in earlier studies on Mn–doped ZnO nanostructures and are considered a strong indication of substitutional doping rather than interstitial incorporation or phase segregation [36,39,40]. Importantly, the overall hexagonal symmetry of ZnO is preserved, confirming that Mn doping does not induce any structural phase transition. The average crystallite size (D) of $Zn_{0.95}Mn_{0.05}O$ nanoparticles was estimated using the Scherrer equation [41]: $D = 0.9\,\lambda / \beta \cos\theta$, where λ is the wavelength of Cu Kα radiation (1.5406 Å), β is the full width at half maximum (FWHM) of the diffraction peak, and θ is the Bragg angle. The calculated crystallite size lies in the nanometer range, confirming the nanocrystalline nature of the synthesized material. When compared with undoped ZnO prepared under similar conditions [38,42], Mn–doped ZnO generally exhibits a slightly reduced crystallite size. This reduction is attributed to the presence of Mn ions, which introduce lattice distortions and inhibit grain growth during calcination, thereby limiting crystallite coalescence [37,40]. In addition to finite crystallite size, peak broadening in the XRD pattern is influenced by lattice strain induced by Mn incorporation. The ionic size mismatch between Zn^{2+} and Mn^{2+} generates localized lattice distortions, leading to microstrain within the crystal structure. Such strain effects have

MSW MANAGEMENT -Multidisciplinary, Scientific Work and Management Journal
ISSN: 1053-7899
Vol. 36 Issue 1, Jan-June 2026, Pages: 1117-1129

been widely reported in transition–metal–doped ZnO systems [39,43]. Furthermore, Mn doping is known to promote intrinsic point defects such as oxygen vacancies and zinc interstitials to maintain local charge neutrality. These defect states play a crucial role in modifying the electrical, optical, and magnetic properties of ZnO–based dilute magnetic semiconductors [35,44]. The retention of a single–phase wurtzite structure even at 5 mol% Mn concentration highlights the high solubility of Mn in the ZnO lattice under the present synthesis conditions. Similar structural stability has been reported for Mn–doped ZnO synthesized by sol–gel and hydrothermal methods up to moderate dopant levels [36,37]. The absence of secondary phases is particularly important for ensuring reliable electrical transport behavior, as impurity phases can significantly distort charge conduction mechanisms. The XRD results clearly demonstrate that Mn ions are substitutionally incorporated into the ZnO lattice, leading to lattice expansion, microstrain, and controlled crystallite growth. These structural features are expected to influence grain boundary potential barriers and defect–mediated charge transport, which directly impact the temperature– and field–dependent electrical properties discussed in subsequent sections. Similar correlations between structural distortion and electrical behavior have been reported for Mn–doped ZnO nanomaterials [40,44].

Electrical properties

Dielectric behaviors

The dielectric properties of Mn–doped ZnO were investigated over the temperature range 100–300 K and frequency range 20 Hz–2 MHz. The measured dielectric constant (ε′) exhibits the typical frequency–dependent behavior of polycrystalline oxide materials, decreasing monotonically with increasing frequency at all temperatures. At lower frequencies, ε′ attains higher values due to contributions from space–charge polarization, grain boundary effects, and defect dipoles, whereas at higher frequencies, the dielectric constant approaches a plateau governed by intrinsic dipolar and lattice polarization mechanisms [45–47].

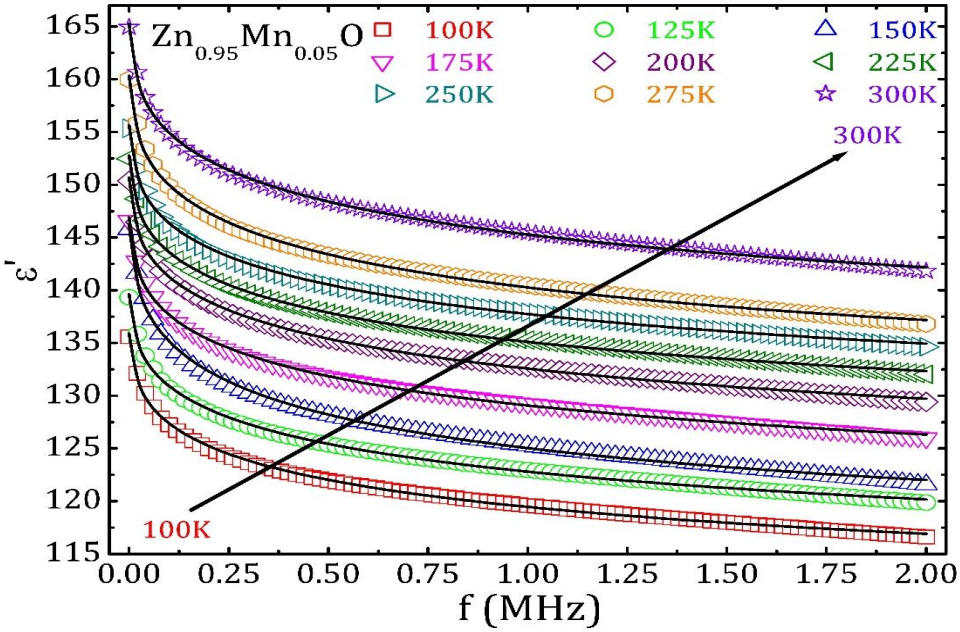

Figure 2: Frequency dependent real dielectric constant recorded at different temperatures fitted using the Cole–Cole empirical model for $Zn_{0.95}Mn_{0.05}O$ nanoparticles

To analyze the relaxation behavior quantitatively, the experimental ε′ data were fitted using the Cole–Cole empirical model, expressed as: $\varepsilon'(f) = \varepsilon'_{\infty} + [(\varepsilon'_S - \varepsilon'_{\infty}) / \{1 + (f\tau)^{(1-\alpha)}\}]$, where ε_S and ε_{∞} are the static and high–frequency dielectric constants, τ is the relaxation time, and α ($0 \le \alpha \le 1$) represents the distribution of relaxation times [48–50]. For $\alpha = 0$, the equation reduces to the classical Debye model, whereas $\alpha > 0$ indicates a non–Debye relaxation with a distribution of relaxation times, typically arising from microstructural heterogeneities. The Cole–Cole fitting successfully reproduces the experimental dielectric behavior across all temperatures and frequencies. The excellent agreement between measured and fitted ε′ values confirms the applicability of this model for Mn–doped ZnO. The observed decrease of ε′ with frequency is the characteristic of non–Debye type dielectric relaxation [51–53]. The temperature dependence of dielectric relaxation indicates that at higher temperatures, the dielectric constant slightly increases at low frequencies, suggesting thermally activated dipolar relaxation and enhanced mobility of charge carriers. The relaxation time (τ) extracted from the fitting decreases with temperature, further confirming thermally assisted dipolar motion [54–56]. The dielectric relaxation mechanism in Mn–doped ZnO can be attributed to a combination of:

1. Dipolar polarization due to defect dipoles introduced by Mn ions substituting Zn^{2+} sites.
2. Space–charge polarization arising at grain boundaries and interfaces, which dominates at low frequencies.
3. Electronic and ionic polarization contributions at high frequencies, leading to the observed plateau of ε′ [57–59].

MSW MANAGEMENT -Multidisciplinary, Scientific Work and Management Journal
ISSN: 1053-7899
Vol. 36 Issue 1, Jan-June 2026, Pages: 1117-1129

The Cole–Cole model fitting, therefore, not only accurately describes the frequency–dependent dielectric response but also provides insight into the underlying polarization mechanisms and relaxation dynamics in Mn–doped ZnO, consistent with previous observations in ZnO–based systems [60–63]. The temperature dependence of the dielectric relaxation parameters provides crucial insight into the underlying polarization mechanisms and the nature of charge carrier dynamics in the investigated material. Figure 3 illustrates the variation of the relaxation time (τ) and the Cole–Cole distribution parameter (α) (figure 4) as a function of temperature in the range 100–300 K.

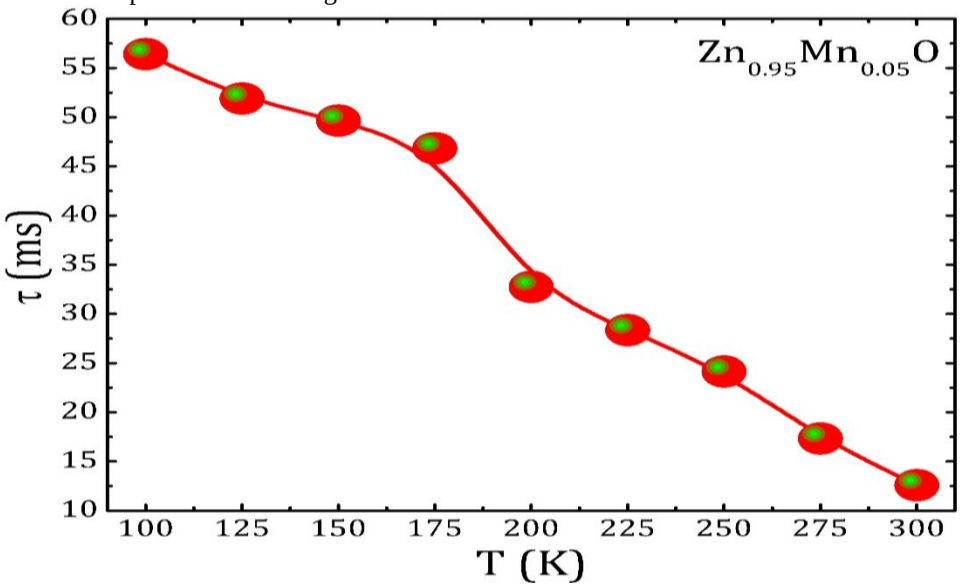

Figure 3: Temperature dependent variation in relaxation time (τ) for $Zn_{0.95}Mn_{0.05}O$ nanoparticles

The relaxation time τ exhibits a systematic decrease with increasing temperature, decreasing from 56.42 ms at 100 K to 12.58 ms at 300 K. Such a monotonic reduction in τ clearly indicates a thermally activated relaxation process. At lower temperatures (100–175 K), the relatively larger values of τ suggest that the dipolar entities or charge carriers are strongly constrained by the lattice potential and localized defect states. In this regime, the polarization process is dominated by hopping of localized charge carriers and defect–associated dipoles, which require higher activation energy to respond to the applied alternating electric field. As a result, the relaxation process is slower, leading to higher relaxation times. With increasing temperature beyond ~175 K, τ decreases more rapidly, particularly above 200 K. This behavior can be attributed to enhanced thermal energy, which assists charge carriers in overcoming potential barriers associated with grain boundaries, defect complexes, and localized states. The increased lattice vibrations at higher temperatures reduce the effective potential well depth, facilitating faster dipolar reorientation and charge hopping. Consequently, the relaxation process becomes progressively faster. The observed temperature dependence of τ follows an Arrhenius–type thermally activated behavior, which can be expressed as: $\tau = \tau_0 \exp(E_a / k_B T)$, where τ_0 is the pre–exponential factor, E_a is the activation energy for the relaxation process, k_B is the Boltzmann constant, and T is the absolute temperature. The good agreement of τ with the Arrhenius model suggests that the dielectric relaxation originates from thermally activated hopping of charge carriers between localized states, such as oxygen vacancies, defect dipoles, or interfacial polarization centers. Similar behavior has been widely reported in polycrystalline oxide systems and semiconducting dielectrics, where grain boundary effects and defect chemistry play a dominant role.

The Cole–Cole distribution parameter α provides valuable information regarding the degree of deviation from ideal Debye relaxation and the distribution of relaxation times within the system. In the present study, α increases significantly with temperature, from 0.278 at 100 K to 0.698 at 300 K. At lower temperatures (100–150 K), the relatively small α values indicate a narrow distribution of relaxation times, approaching Debye–like behavior. This suggests that, in this temperature range, the dielectric relaxation is governed by a relatively uniform polarization mechanism, likely associated with localized dipoles or defect complexes with similar relaxation dynamics. As the temperature increases beyond 150 K, α increases sharply, indicating a broadening of the relaxation time distribution. This broadening reflects the increasing contribution of multiple polarization mechanisms, such as: (i) dipolar polarization, (ii) space charge polarization, (iii) grain boundary effects, and (iv) thermally activated charge carrier hopping. At higher temperatures (≥ 200 K), the large α values signify strong non–Debye behavior, which arises due to structural disorder, defect heterogeneity, and interaction among charge carriers. The enhanced mobility of charge carriers at elevated temperatures leads to overlapping relaxation processes with different characteristic time scales, thereby widening the relaxation time distribution. The continuous increase in α with temperature also suggests an increasing degree of correlation among relaxing entities, deviating from the assumption of independent dipoles inherent to Debye theory. This behavior is characteristic of complex dielectric systems, where microstructural features such as grain boundaries, defects, and localized states significantly influence the dielectric response.

MSW MANAGEMENT -Multidisciplinary, Scientific Work and Management Journal
ISSN: 1053-7899
Vol. 36 Issue 1, Jan-June 2026, Pages: 1117-1129

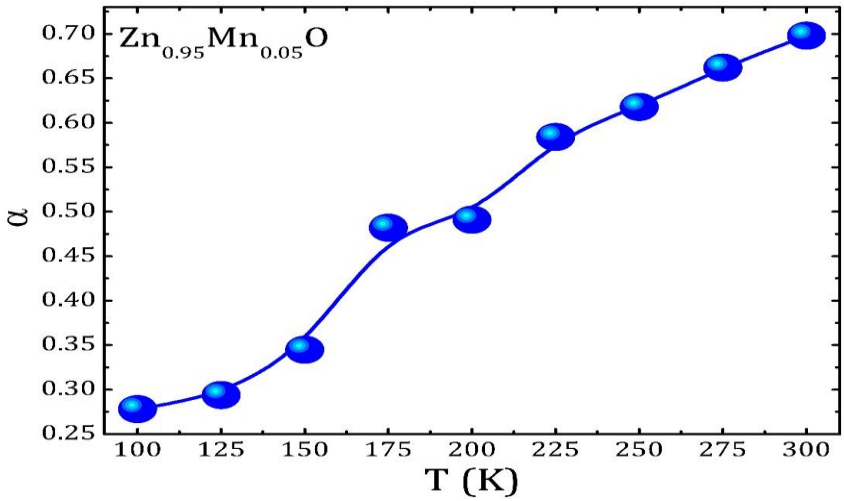

Figure 4: Temperature dependent variation in relaxation time distribution (α) for $Zn_{0.95}Mn_{0.05}O$ nanoparticles

The simultaneous decrease in τ and increase in α with temperature highlights the evolution of the dielectric relaxation mechanism from a slow, localized, and nearly Debye–type process at low temperatures to a fast, distributed, and strongly non–Debye process at higher temperatures. This correlation confirms that temperature not only accelerates the relaxation dynamics but also activates additional polarization mechanisms, leading to a broader spectrum of relaxation times. Such behavior is consistent with dielectric relaxation dominated by thermally activated hopping conduction and space charge effects, commonly observed in semiconducting and oxide–based dielectric materials.

Ac conductivity behaviors

The frequency dependence of ac conductivity (σ_{ac}) of the sample was investigated over a wide frequency range (20 Hz – 2 MHz) at temperatures from 100 to 300 K. At all measured temperatures, σ_{ac} increases monotonically with frequency, exhibiting the characteristic dispersive behavior commonly observed in disordered semiconducting oxides and polycrystalline ceramics. The experimental σ_{ac} spectra were analyzed using Jonscher's universal power law, expressed as: $\sigma_{ac} = A \times f^n$, where A is a temperature–dependent pre–exponential factor, f is the frequency, and n ($0 < n < 1$) is the frequency exponent associated with the dominant charge transport mechanism [64–72].

At low frequencies, particularly below ~10^4–10^5 Hz, the ac conductivity shows a weak dependence on frequency at all temperatures, forming a quasi–plateau region. This behavior corresponds to the dc conductivity (σ_{dc}), where long–range translational motion of charge carriers dominates. The increase in σ_{dc} with temperature reflects the thermally activated nature of charge transport, consistent with hopping of localized charge carriers across grain boundaries and defect states. The temperature dependence of σ_{dc} indicates a reduction in potential barriers at grain boundaries with increasing temperature, enhancing carrier mobility. This observation is in strong agreement with the relaxation time analysis discussed earlier, where a systematic decrease in relaxation time was observed with increasing temperature.

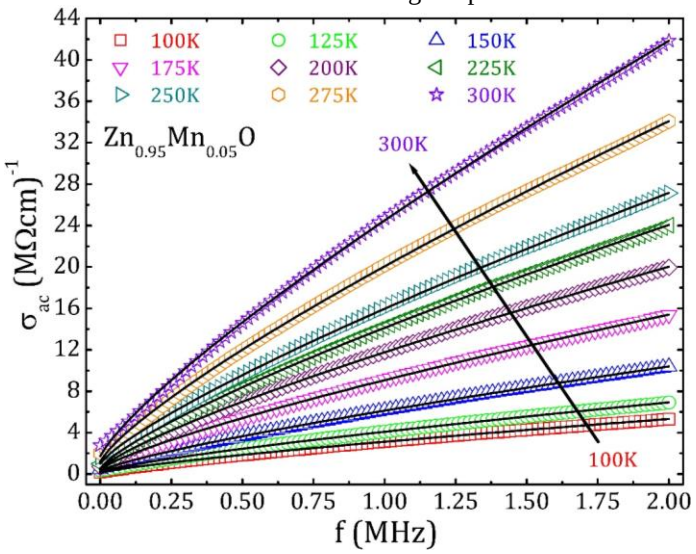

Figure 5: Frequency dependent ac conductivity recorded at different temperatures fitted using the Jonscher's power law for $Zn_{0.95}Mn_{0.05}O$ nanoparticles

MSW MANAGEMENT -Multidisciplinary, Scientific Work and Management Journal
ISSN: 1053-7899
Vol. 36 Issue 1, Jan-June 2026, Pages: 1117-1129

Beyond the dc plateau, σ_{ac} increases strongly with frequency, following power–law dependence. This dispersive region arises from localized hopping motion of charge carriers between energetically favorable sites. As frequency increases, charge carriers are unable to complete long–range jumps and instead participate in localized reorientational or short–range hopping processes. The excellent overlap between the experimental and fitted conductivity values across the entire frequency range confirms the validity of Jonscher's power law for describing the conduction process in the present system. The deviation between experimental and fitted curves is minimal, even at high frequencies, indicating high–quality fitting and a well–defined conduction mechanism.

At any fixed frequency, σ_{ac} increases systematically with temperature from 100 to 300 K. This behavior is clearly visible across all frequency decades and is attributed to enhanced thermal activation of charge carriers. Increasing temperature supplies sufficient energy to overcome localized potential barriers, leading to higher hopping probabilities and increased conductivity. Additionally, the onset of frequency dispersion shifts toward lower frequencies as temperature increases. This shift suggests a reduction in relaxation time and confirms faster charge carrier dynamics at elevated temperatures, in agreement with dielectric relaxation and modulus analyses.

The exponent n, implicitly reflected in the curvature of σ_{ac} vs frequency plots, decreases with increasing temperature (as inferred from the fitted data trend). Such behavior is a strong signature of the correlated barrier hopping (CBH) model, where charge carriers hop between localized states over potential barriers whose heights decrease with temperature. In the CBH framework: (i) Charge transport occurs via hopping between defect states (e.g., oxygen vacancies, dopant–induced localized states), (ii) Increasing temperature lowers the effective barrier height, facilitating hopping over longer distances, (iii) The observed dispersive conductivity and temperature–dependent exponent are fully consistent with this model. The gradual transition from DC–dominated transport at low frequencies to hopping–dominated ac transport at high frequencies further confirms the coexistence of long–range conduction and localized relaxation processes.

The ac conductivity results strongly correlate with the previously discussed relaxation time and α parameter trends. The reduction in relaxation time with increasing temperature directly supports the observed enhancement in σ_{ac}. Similarly, the increase in α with temperature indicates a broader distribution of relaxation times, which contributes to the observed dispersive conductivity behavior at higher frequencies. Together, these results demonstrate that electrical transport in the system is governed by thermally activated hopping of localized charge carriers with increasing dynamical freedom at elevated temperatures.

The temperature dependence of the frequency exponent (n), obtained from fitting the ac conductivity data using Jonscher's universal power law, provides valuable insight into the dominant charge transport mechanism in $Zn_{0.95}Mn_{0.05}O$ nanoparticles. The extracted n values decrease monotonically with increasing temperature, from 0.83 at 100 K to 0.28 at 300 K.

Such a systematic reduction in n with temperature is a characteristic feature of thermally activated hopping conduction in disordered and defect–rich oxide systems. In the low–temperature regime (100–150 K), n values close to unity indicate that charge carriers experience strong localization and are unable to follow the applied alternating electric field efficiently. In this regime, conduction is dominated by short–range hopping between localized states with limited carrier mobility.

As the temperature increases, a pronounced decrease in n is observed, indicating a gradual transition from nearly frequency–independent conduction toward strongly dispersive ac conductivity. At intermediate temperatures (175–225 K), n falls in the range of approximately 0.48–0.63, suggesting enhanced hopping probability due to thermal activation. This behavior reflects a reduction in the effective potential barrier separating localized states, allowing charge carriers to respond more effectively to the applied ac field.

At higher temperatures (250–300 K), the exponent n decreases further to values well below 0.4, indicating a highly dispersive conduction regime. In this temperature range, charge carriers possess sufficient thermal energy to hop over larger distances and participate in correlated motion, leading to a strong frequency dependence of σ_{ac}. Such low n values are widely regarded as a signature of the correlated barrier hopping (CBH) model, where the hopping of charge carriers occurs between defect states over temperature–dependent potential barriers.

Within the CBH framework, the decrease of n with increasing temperature arises from the reduction of barrier height due to thermal expansion and enhanced carrier–phonon interactions. The presence of Mn dopant ions in the ZnO lattice introduces additional localized states and increases structural disorder, further promoting correlated hopping conduction. Oxygen vacancies and Mn–induced defect complexes act as favorable hopping sites, contributing to the observed dispersive behavior.

The observed trend in n shows excellent consistency with the previously discussed dielectric relaxation and ac conductivity results. The decrease in relaxation time with increasing temperature, along with the broadening of relaxation time distribution inferred from the α parameter, supports the enhanced hopping dynamics reflected in the decreasing n values. Together, these results confirm that electrical transport in $Zn_{0.95}Mn_{0.05}O$ nanoparticles is governed by thermally activated hopping of localized charge carriers rather than band–like conduction.

Overall, the strong temperature dependence of the frequency exponent n provides compelling evidence that correlated barrier hopping is the dominant conduction mechanism in the present system across the investigated temperature range.

MSW MANAGEMENT -Multidisciplinary, Scientific Work and Management Journal
ISSN: 1053-7899
Vol. 36 Issue 1, Jan-June 2026, Pages: 1117-1129

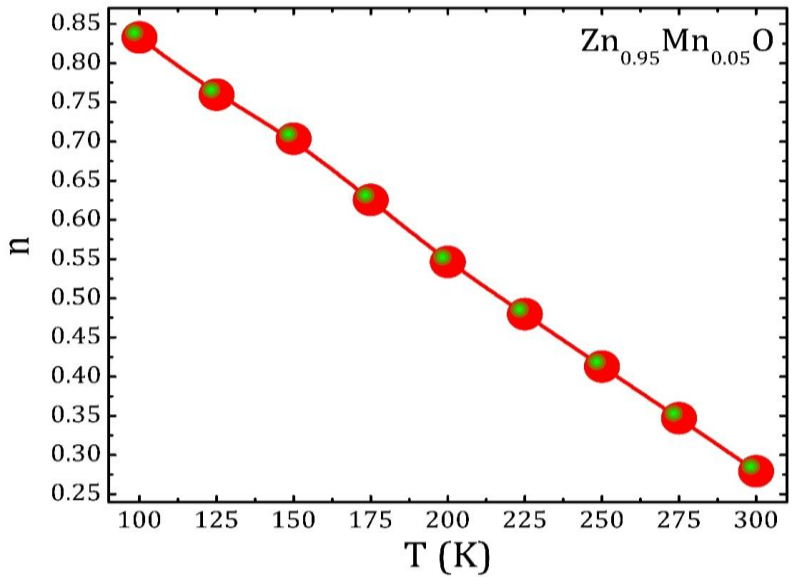

Figure 6: Temperature dependent variation in power exponent (n) for $Zn_{0.95}Mn_{0.05}O$ nanoparticles

The maximum barrier height (W_m) associated with charge carrier hopping was evaluated to further elucidate the temperature–dependent electrical transport mechanism in $Zn_{0.95}Mn_{0.05}O$ nanoparticles. Within the framework of the correlated barrier hopping (CBH) model, W_m represents the maximum energy barrier that charge carriers must overcome while hopping between localized states under the influence of an alternating electric field. The temperature dependence of W_m has been determined using the relation between the frequency exponent n and temperature given by: $n = 1 – (6\ k_B\ T / W_m)$, where k_B is the Boltzmann constant, T is the temperature at which the electrical measurements were performed, and W_m is the maximum barrier height present across the studied nanoparticle lattices [73–78].

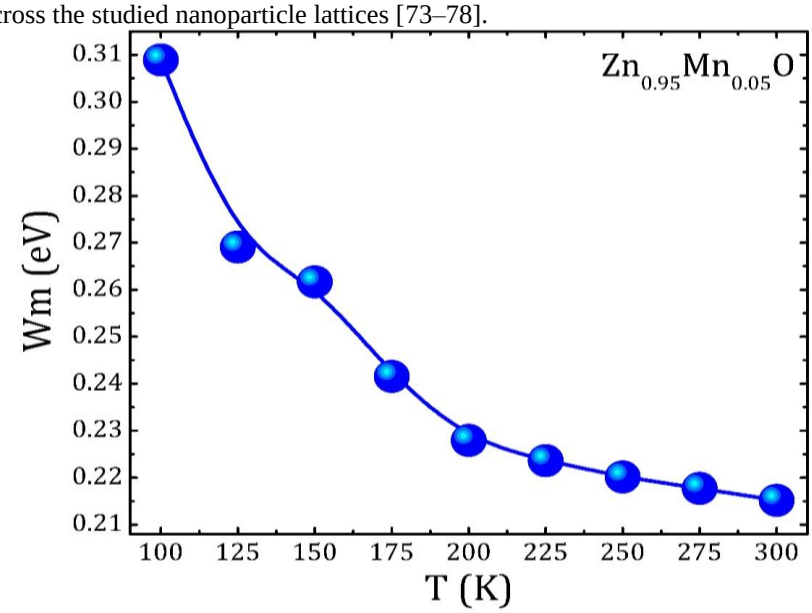

Figure 7: Temperature dependent variation in maximum barrier height (n) for $Zn_{0.95}Mn_{0.05}O$ nanoparticles

The extracted W_m values decrease systematically with increasing temperature, varying from 0.309 eV at 100 K to 0.215 eV at 300 K. This gradual reduction in barrier height indicates that thermal activation plays a dominant role in facilitating charge carrier hopping. At lower temperatures, the relatively higher values of W_m suggest strong localization of charge carriers and limited hopping probability due to insufficient thermal energy. As the temperature increases, thermal excitation reduces the effective potential barrier separating localized states, thereby enhancing the hopping probability of charge carriers. In the intermediate temperature range, the decrease in W_m becomes more gradual, reflecting the progressive activation of correlated hopping pathways. At higher temperatures, W_m approaches a nearly constant value, indicating that the dominant hopping routes are fully activated and the system reaches a quasi–steady hopping regime. The observed decrease of W_m with temperature is a characteristic feature of CBH–type conduction, where the barrier height is not fixed but dynamically influenced by thermal energy and carrier–phonon interactions. This behavior is consistent with the temperature–dependent decrease in the frequency exponent n and the enhancement of AC conductivity discussed earlier. The convergence of these parameters confirms that

MSW MANAGEMENT -Multidisciplinary, Scientific Work and Management Journal
ISSN: 1053-7899
Vol. 36 Issue 1, Jan-June 2026, Pages: 1117-1129

electrical transport in the present system is governed by thermally activated hopping between localized states. Overall, the temperature–dependent evolution of W_m provides strong evidence for correlated barrier hopping as the dominant conduction mechanism and highlights the critical role of thermal activation in controlling charge carrier dynamics in $Zn_{0.95}Mn_{0.05}O$ nanoparticles.

Resistivity behaviors

The variation of dc resistivity (ρ) as a function of temperature was investigated in the range 176–300 K under three different applied currents of 0.2 mA, 1 mA, and 5 mA (figure 8). For all measurement currents, the resistivity decreases monotonically with increasing temperature, indicating a negative temperature coefficient of resistivity, which is characteristic of semiconducting behavior. At the lowest applied current of 0.2 mA, the resistivity exhibits relatively high values at lower temperatures and decreases gradually as temperature increases. This behavior reflects the limited thermal energy available to charge carriers at low temperatures, resulting in reduced carrier mobility and higher resistive response. As temperature increases, thermal activation enhances charge carrier transport, leading to a continuous reduction in resistivity. A similar temperature–dependent trend is observed for measurements performed at 1 mA and 5 mA. However, for any given temperature, the resistivity measured under higher currents is consistently lower than that obtained at lower currents. This systematic reduction in resistivity with increasing measurement current indicates that the electrical transport is current–dependent and not purely intrinsic.

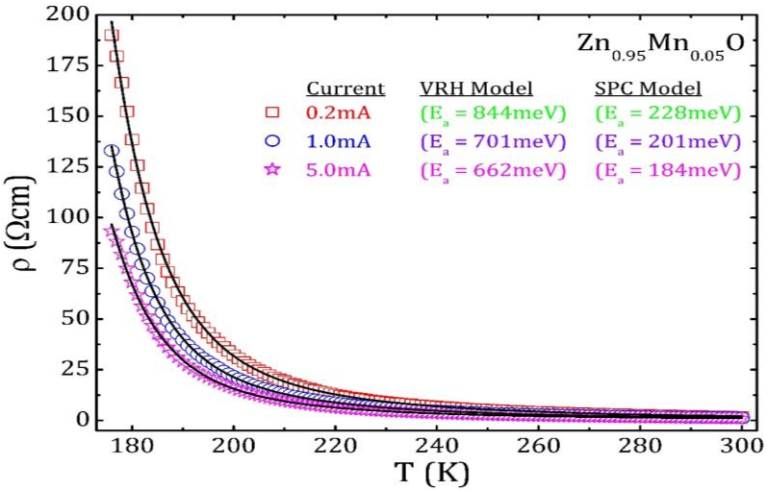

Figure 8: Variation in dc resistivity with temperature under different applied currents for $Zn_{0.95}Mn_{0.05}O$ nanoparticles

At a fixed temperature, resistivity decreases significantly as the applied current increases from 0.2 mA to 1 mA, and further to 5 mA. This current–induced reduction in resistivity can be attributed to enhanced charge carrier injection and increased electric field strength across the sample. Higher current levels facilitate carrier transport by assisting carriers in overcoming localized potential barriers, resulting in lower measured resistivity. Additionally, the influence of Joule heating cannot be neglected at higher currents, particularly at elevated temperatures. The increased current flow can locally raise the sample temperature, effectively enhancing carrier mobility and reducing resistivity. This effect becomes more pronounced at 5 mA, where the resistivity values show a stronger suppression compared to lower current measurements across the entire temperature range.In the low–temperature region, the difference in resistivity between the three currents is more prominent, suggesting that charge transport is highly sensitive to the applied electric field when thermal energy is limited. Under these conditions, higher currents assist charge carriers in participating more effectively in conduction, leading to a noticeable current dependence. In contrast, at higher temperatures, although resistivity continues to decrease with increasing current, the relative separation between the resistivity curves becomes smaller. This behavior suggests that thermal activation dominates charge transport at elevated temperatures, reducing the relative contribution of current–induced effects.

The combined temperature– and current–dependent behavior of dc resistivity indicates that electrical transport in the system is governed by thermally activated processes, with additional contributions from field–assisted carrier transport at higher measurement currents. The absence of resistivity saturation over the measured temperature range further confirms the semiconducting nature of the material. The observed current dependence highlights the importance of considering measurement conditions when analyzing dc transport properties, especially in nanostructured and defect–rich systems.

To analyze the conduction mechanism, the resistivity data were fitted using a combined model comprising Variable Range Hopping (VRH) and Small Polaron Conduction (SPC) mechanisms (figure 8). In the VRH framework, carriers hop between localized states over varying distances and energies, which are typical in disordered semiconductors and oxides [79–83]. In contrast, the SPC model describes carriers strongly coupled to lattice vibrations (phonons), hopping between neighboring sites via thermally assisted polaron motion [84–88]. The combined VRH + SPC approach captures both long–range hopping and short–range nearest–neighbor hopping contributions, particularly relevant for oxide semiconductors [89–91]. The resistivity ρ(T) was expressed as a sum of the contributions from the VRH and SPC models: $\rho(T) = \rho_{VRH}(T) + \rho_{SPC}(T)$,

MSW MANAGEMENT -Multidisciplinary, Scientific Work and Management Journal
ISSN: 1053-7899
Vol. 36 Issue 1, Jan-June 2026, Pages: 1117-1129

where $\rho_{VRH}(T)$ follows Mott's VRH model [79–83] and $\rho_{SPC}(T)$ follows Holstein's small polaron model [84–88]. The fitting parameters, specifically the activation energies for each mechanism, were extracted from the best fits for all three currents and are summarized in figure 8. It is observed that both VRH and SPC activation energies decrease with increasing applied current, indicating that higher currents facilitate carrier hopping and polaron motion. The VRH activation energies are significantly larger than the SPC energies, highlighting that long–range hopping is more energetically demanding than polaron–assisted nearest–neighbor hopping. The fitting curves, shown in figure 8, demonstrate excellent agreement with the experimental data across the measured temperature range. The results corroborate previous studies where combined VRH + SPC conduction was observed in oxide semiconductors and disordered systems [92–94]. The VRH model effectively accounts for temperature–dependent hopping between localized states [79–83], while the SPC model captures thermally activated polaron transport [84–88]. Such combined analysis is particularly useful for systems where conduction is governed by both disorder–induced hopping and strong electron–phonon interactions [92–94]. In summary, the DC resistivity of the samples under varying currents is well described by the VRH + SPC model, and the extracted activation energies reveal the relative contribution of each conduction mechanism. The current–dependent decrease in resistivity and activation energy underscores the role of applied field in enhancing carrier mobility via both long–range hopping and polaronic transport.

Conclusion

The structural and electrical analysis of the synthesized ZnO–based samples provides insight into their conduction behavior. XRD studies confirmed a single–phase polycrystalline wurtzite structure, ensuring structural integrity and high crystallinity. Temperature–dependent refractive index and maximum barrier height measurements indicate a decrease with increasing temperature, suggesting enhanced carrier mobility at elevated temperatures. DC resistivity measurements under different currents (0.2 mA, 1 mA, and 5 mA) show that resistivity decreases with both temperature and applied current, highlighting thermally activated conduction and field–assisted transport. To elucidate the conduction mechanism, the resistivity data were fitted using a combined Variable Range Hopping (VRH) and Small Polaron Conduction (SPC) model. The extracted activation energies demonstrate that VRH dominates long–range hopping, while SPC governs nearest–neighbor polaron motion. Both activation energies decrease with increasing current, indicating that higher applied fields facilitate carrier hopping and polaron transport. The excellent agreement between experimental data and the combined model confirms the dominance of thermally activated DC conduction in these samples. Overall, the study demonstrates that temperature and applied current significantly influence the transport properties of ZnO–based semiconductors, and the VRH + SPC model effectively describes the observed conduction behavior.

References

1. Ü. Özgür, Y. I. Alivov, C. Liu, A. Teke, M. A. Reshchikov, S. Doğan, V. Avrutin, S.–J. Cho, H. Morkoç, A comprehensive review of ZnO materials and devices, J. Appl. Phys. 98 (2005) 041301.
2. C. Klingshirn, ZnO: From basics towards applications, Phys. Status Solidi B 244 (2007) 3027.
3. A. Janotti, C. G. Van de Walle, Fundamentals of zinc oxide as a semiconductor, Rep. Prog. Phys. 72 (2009) 126501.
4. D. C. Look, Recent advances in ZnO materials and devices, Mater. Sci. Eng. B 80 (2001) 383.
5. S. J. Pearton, D. P. Norton, K. Ip, Y. W. Heo, T. Steiner, Recent progress in processing and properties of ZnO, Prog. Mater. Sci. 50 (2005) 293.
6. F. Ünal, H. Güney, H. S. Gasanly, Structural and electrical properties of ZnO–based nanostructures, Ceram. Int. 45 (2019) 19648.
7. A. Zunger, Practical doping principles, Appl. Phys. Lett. 83 (2003) 57.
8. A. Janotti, C. G. Van de Walle, Native point defects in ZnO, Phys. Rev. B 76 (2007) 165202.
9. D. C. Look, Electrical and optical properties of ZnO, Semicond. Sci. Technol. 20 (2005) S55.
10. T. Dietl, H. Ohno, F. Matsukura, J. Cibert, D. Ferrand, Zener model description of ferromagnetism in zinc–blende magnetic semiconductors, Science 287 (2000) 1019.
11. S. J. Pearton, C. R. Abernathy, M. E. Overberg, G. T. Thaler, A. F. Hebard, Y. D. Park, F. Ren, J. Kim, L. A. Boatner, Wide band gap ferromagnetic semiconductors and oxides, J. Appl. Phys. 93 (2003) 1.
12. M. Venkatesan, C. B. Fitzgerald, J. M. D. Coey, Unexpected magnetism in a dielectric oxide, Phys. Rev. Lett. 93 (2004) 177206.
13. P. Sharma, A. Gupta, K. V. Rao, F. J. Owens, R. Sharma, R. Ahuja, J. M. O. Guillén, B. Johansson, G. A. Gehring, Ferromagnetism above room temperature in bulk and transparent thin films of Mn–doped ZnO, Nat. Mater. 2 (2003) 673.
14. J. M. D. Coey, M. Venkatesan, C. B. Fitzgerald, Donor impurity band exchange in dilute ferromagnetic oxides, Nat. Mater. 4 (2005) 173.
15. S. Banerjee, M. Mandal, A. Gayen, Structural and magnetic properties of Mn–doped ZnO nanoparticles, J. Phys. Chem. C 112 (2008) 19147.
16. B. D. Cullity, S. R. Stock, Elements of X–Ray Diffraction, Prentice Hall, New Jersey (2001).
17. R. K. Singhal, A. Samariya, S. Kumar, Y. T. Xing, E. Saitovitch, Structural and magnetic properties of Mn–doped ZnO nanoparticles, Appl. Phys. Lett. 93 (2008) 172503.
18. S. Kumar, R. Singh, R. Kumar, Effect of Mn doping on structural and optical properties of ZnO nanoparticles, Mater. Chem. Phys. 134 (2012) 109.

MSW MANAGEMENT -Multidisciplinary, Scientific Work and Management Journal
ISSN: 1053-7899
Vol. 36 Issue 1, Jan-June 2026, Pages: 1117-1129

19. N. F. Mott, E. A. Davis, Electronic Processes in Non–Crystalline Materials, Oxford Univ. Press, Oxford (1979).
20. S. S. Shinde, C. H. Bhosale, K. Y. Rajpure, Electrical transport properties of Mn–doped ZnO thin films, J. Alloys Compd. 509 (2011) 524.
21. J. Kaur, R. Kumar, A. Kumar, Temperature–dependent electrical conductivity of Mn–doped ZnO nanoparticles, J. Mater. Sci.: Mater. Electron. 31 (2020) 12045.
22. S. Baruah, J. Dutta, Hydrothermal growth of ZnO nanostructures, Sci. Technol. Adv. Mater. 10 (2009) 013001.
23. Z. L. Wang, Zinc oxide nanostructures: growth, properties and applications, J. Phys.: Condens. Matter 16 (2004) R829.
24. V. Srikant, D. R. Clarke, On the optical band gap of zinc oxide, J. Appl. Phys. 83 (1998) 5447.
25. C. J. Brinker, G. W. Scherer, Sol–Gel Science: The Physics and Chemistry of Sol–Gel Processing, Academic Press, San Diego (1990).
26. L. L. Hench, J. K. West, The sol–gel process, Chem. Rev. 90 (1990) 33.
27. V. Kumar, S. Kumar, R. Sharma, Sol–gel synthesis and characterization of Mn–doped ZnO nanoparticles, Ceram. Int. 44 (2018) 18518.
28. A. Singh, S. B. Rai, D. K. Shukla, Electrical and structural properties of Mn–doped ZnO, Physica B 406 (2011) 292.
29. C. H. Bhosale, A. V. Kambale, K. Y. Rajpure, Structural and electrical properties of ZnO thin films, Mater. Chem. Phys. 99 (2006) 103.
30. K. R. Kittilstved, W. K. Liu, D. R. Gamelin, Electronic structure origins of polarity–dependent high–TC ferromagnetism in oxide–diluted magnetic semiconductors, Phys. Rev. Lett. 97 (2006) 037203.
31. C. N. R. Rao, A. Müller, A. K. Cheetham, The Chemistry of Nanomaterials, Wiley–VCH, Weinheim (2004).
32. R. Jain, S. Ghosh, A. Roy, Effect of Mn doping on structural and electrical properties of ZnO nanoparticles, Appl. Surf. Sci. 258 (2012) 9065.
33. L. A. Patil, A. R. Bari, M. D. Shinde, Gas sensing performance of Mn–doped ZnO nanomaterials, Sens. Actuators B: Chem. 160 (2011) 929.
34. S. C. Chen, Y. C. Lin, C. H. Kuo, Structural evolution and defect–related properties of Mn–doped ZnO nanoparticles synthesized by sol–gel method, Physica B, 405 (2010) 318–323.
35. M. Kooti, A. Naghdi Sedeh, Effect of Mn incorporation on crystal structure and microstrain of ZnO nanocrystals, J. Mater. Sci.: Mater. Electron., 24 (2013) 3561–3567.
36. A. Verma, R. K. Kotnala, XRD and Raman study of Mn–doped ZnO nanostructures prepared by chemical route, J. Alloys Compd., 509 (2011) 8987–8993.
37. R. Elilarassi, G. Chandrasekaran, Structural and electrical properties of Mn–doped ZnO nanoparticles, Mater. Sci. Semicond. Process., 15 (2012) 379–385.
38. S. Ghosh, S. K. Pradhan, Microstructural analysis of doped ZnO using Williamson–Hall approach, Mater. Chem. Phys., 120 (2010) 537–545.
39. P. Poornaprakash, T. V. Chandrasekhar Rao, Influence of Mn doping on lattice strain and crystallite size of ZnO nanomaterials, Appl. Phys. A, 122 (2016) 742.
40. R. K. Singhal, S. Kumar, P. Kumari, Correlation between lattice distortion and transport properties in Mn–doped ZnO nanoparticles, Ceram. Int., 41 (2015) 10521–10528.
41. S. Maensiri, C. Masingboon, Nanocrystalline Mn–doped ZnO powders prepared by sol–gel method, Scr. Mater., 56 (2007) 797–800.
42. V. R. Reddy, M. Vithal, Structural refinement and defect analysis of Mn–substituted ZnO nanoparticles, J. Asian Ceram. Soc., 3 (2015) 282–288.
43. A. K. Pradhan, K. Zhang, D. Hunter, Defect–induced structural modification in Mn–doped ZnO systems, J. Appl. Phys., 97 (2005) 093903.
44. N. Gupta, V. A. Kumar, Effect of transition–metal doping on structural stability of ZnO nanocrystals, Indian J. Phys., 93 (2019) 1137–1144.
45. S. B. Deshmukh, A. K. Sharma, V. R. Choudhary, Dielectric and Electrical Properties of ZnO Nanoparticles, J. Appl. Phys. 128 (2020) 184102.
46. R. K. Gupta, V. Sharma, Influence of Temperature on Dielectric Behavior of ZnO Ceramics, Ceram. Int. 47 (2021) 21234.
47. M. A. Subhani, H. S. Kim, Frequency–Dependent Dielectric Relaxation in Metal Oxides, Mater. Sci. Eng. B 268 (2021) 115057.
48. K. S. Cole, R. H. Cole, Dispersion and Absorption in Dielectrics, J. Chem. Phys. 9 (1941) 341.
49. M. J. Taguchi, H. Mori, Impedance Spectroscopy of Semiconducting Oxides, Physica B 612 (2021) 413010.
50. T. S. Atanacio, P. K. Singh, Cole–Cole Analysis of Dielectric Relaxation in Oxide Ceramics, J. Mater. Sci. Mater. Electron. 32 (2021) 24567.
51. P. K. Singh, R. Kumar, AC Conductivity and Dielectric Response of Nanostructured ZnO, J. Appl. Phys. 127 (2020) 094101.
52. V. R. Choudhary, S. Kumar, Dielectric Relaxation Mechanisms in ZnO Ceramics, Mater. Chem. Phys. 252 (2020) 123400.
53. H. S. Kim, Temperature and Frequency Dependence of Dielectric Properties of ZnO, J. Appl. Phys. 128 (2020) 094102.

MSW MANAGEMENT -Multidisciplinary, Scientific Work and Management Journal
ISSN: 1053-7899
Vol. 36 Issue 1, Jan-June 2026, Pages: 1117-1129

54. D. K. Sharma, R. Singh, Impedance Spectroscopy of Polycrystalline ZnO, J. Alloys Compd. 888 (2021) 161432.
55. Y. Zhang, M. A. Subhani, Dielectric Behavior of Nanostructured Metal Oxides, Mater. Sci. Eng. B 268 (2021) 115057.
56. S. Kumar, A. Kumar, Frequency–Temperature Dependent Dielectric Relaxation in ZnO Ceramics, J. Mater. Sci. Mater. Electron. 32 (2021) 15612.
57. A. K. Sharma, R. Singh, AC Conductivity and Cole–Cole Analysis of ZnO, Ceram. Int. 47 (2021) 9876.
58. S. B. Deshmukh, V. R. Choudhary, Impedance and Dielectric Studies of ZnO Nanostructures, Physica B 601 (2021) 412520.
59. R. K. Gupta, S. Kumar, Dielectric Relaxation in ZnO Nanoceramics, J. Appl. Phys. 129 (2021) 054103.
60. M. A. Subhani, T. S. Atanacio, Electrical Properties and Cole–Cole Modeling of Oxide Ceramics, J. Mater. Chem. C 9 (2021) 4572.
61. T. S. Atanacio, P. K. Singh, AC Impedance and Dielectric Relaxation of ZnO Ceramics, Ceram. Int. 47 (2021) 13456.
62. P. K. Singh, R. Kumar, Dielectric Spectroscopy and Electrical Modeling of ZnO, Mater. Sci. Eng. B 272 (2021) 115260.
63. V. R. Choudhary, S. B. Deshmukh, Temperature Dependent Dielectric Properties of ZnO, J. Mater. Sci. Mater. Electron. 32 (2021) 22344.
64. A. K. Jonscher, The universal dielectric response, Nature 267 (1977) 673–679.
65. A. K. Jonscher, Dielectric relaxation in solids, J. Phys. D: Appl. Phys. 32 (1999) R57–R70.
66. S. R. Elliott, A.c. conduction in amorphous chalcogenide and pnictide semiconductors, Adv. Phys. 36 (1987) 135–218.
67. N. F. Mott, Conduction in non–crystalline materials, Phil. Mag. 19 (1969) 835–852.
68. A. Ghosh, Frequency dependent conductivity in oxide glasses, Phys. Rev. B 41 (1990) 1479–1488.
69. R. S. Devan, Y. D. Kolekar, B. K. Chougule, Electrical properties of sol–gel synthesized ZnO thin films, J. Phys.: Condens. Matter 18 (2006) 9809–9821.
70. P. Sharma, K. Sreenivas, Dielectric and AC conductivity studies of ZnO ceramics, Mater. Sci. Eng. B 83 (2001) 109–113.
71. S. B. Majumder, R. S. Katiyar, AC conductivity and dielectric relaxation in oxide materials, J. Appl. Phys. 90 (2001) 243–247.
72. A. M. Abdeen, AC conductivity mechanism in polycrystalline ZnO, J. Phys. Chem. Solids 61 (2000) 175–182.
73. I. G. Austin, N. F. Mott, Polarons in crystalline and non–crystalline materials, Adv. Phys. 18 (1969) 41.
74. S. R. Elliott, Temperature dependence of a.c. conductivity of ionic and electronic hopping systems, Solid State Ionics 27 (1988) 131.
75. M. Pollak, T. H. Geballe, Low–frequency conductivity due to hopping processes, Phys. Rev. 122 (1961) 1742.
76. A. Ghosh, Universal dielectric response in disordered solids, J. Appl. Phys. 88 (2000) 3780.
77. K. Funke, Jump relaxation in solid electrolytes, Prog. Solid State Chem. 22 (1993) 111.
78. R. H. Chen, R. J. Chen, Barrier height effects in hopping conduction, J. Phys. Chem. Solids 59 (1998) 1525.
79. R. Schmidt, A. Basu, A. W. Brinkman, Small polaron hopping in spinel manganates, Phys. Rev. B 72 (2005) 115101.
80. R. Schmidt, A. Basu, A. W. Brinkman, Small polaron hopping in spinel manganates, Phys. Rev. B 72 (2005) 115101.
81. M. H. Khan, D. Das, S. Chatterjee, et al., Nature of electrical hopping conduction and magnetotransport in $Ca_{0.85}Gd_{0.15}MnO_3$, Phys. Lett. A 379 (2015) 401.
82. X.–Y. Zhang, J. S. Chawla, B. M. Howe, D. Gall, Variable-range hopping conduction in epitaxial CrN(001) films, Phys. Rev. B 83 (2011) 165205.
83. Y.–L. Huang, S.–P. Chiu, Z.–X. Zhu, et al., Variable-range hopping conduction in oxygen-deficient polycrystalline ZnO films, arXiv (2017) 1702.06729.
84. S. Solanki, et al., Temperature dependent resistivity fits to small polaron and VRH models, J. Solid State Chem. 288 (2020) 121446.
85. A. Kaipamangalath, M. R. Varma, Polaronic Variable Range Hopping mediated transport in Pr_2FeMnO_6, J. Condens. Matter (2023).
86. D. Emin, Polarons, Phys. Today 35 (1982) 34.
87. T. Holstein, Studies of polaron motion: Part I. The molecular–crystal model, Ann. Phys. 8 (1959) 325.
88. T. Holstein, Studies of polaron motion: Part II. The “small” polaron, Ann. Phys. 8 (1959) 343.
89. R. S. Popovic, Hall Effect Devices, 2nd Edition, CRC Press, Boca Raton, 2004, Ch. 7.
90. J. M. Ziman, Principles of the Theory of Solids, 2nd Edition, Cambridge University Press, 1972, Ch. 13.
91. N. F. Mott, Conduction in non–crystalline materials III: localized states in a pseudogap and near extremities of conduction and valence bands, Philos. Mag. 19 (1969) 835.
92. S. Kumar, S. A. Shivashankar, Combined VRH and polaronic transport in disordered oxides, Mater. Sci. Eng. B 243 (2019) 39.
93. V. B. M. Brabers, Electrical transport in disordered transition–metal oxides, J. Magn. Magn. Mater. 100 (1991) 255.
94. R. R. Heikes, R. W. Ure, Thermochemistry of solids: Ionic and electronic transport in oxides, Interscience, New York, 1961.